Received: 11 October 2024 | Revised: 10 February 2025 | Accepted: 13 February 2025
DOI: 10.1002/inf2.70010

RESEARCH ARTICLE

WILEY

Semiconductor-to-metal transition in platinum dichalcogenides induced by niobium dichalcogenides

Lei Zhang[1] | **Xin Zhou**[2] | **Tong Yang**[3] | **Yuan Chen**[1] | **Fangjie Wang**[1] | **Haoge Cheng**[1] | **Dechun Zhou**[1] | **Goki Eda**[1] | **Zheng Liu**[2] | **Andrew T. S. Wee**[1]

[1]Department of Physics, National University of Singapore, Singapore, Singapore
[2]School of Materials Science and Engineering, Nanyang Technological University, Singapore, Singapore
[3]Department of Applied Physics, The Hong Kong Polytechnic University, Hong Kong SAR, the People's Republic of China

Correspondence
Lei Zhang, Department of Physics, National University of Singapore, 2 Science Drive 3, Singapore 117551, Singapore.
Email: zlei@u.nus.edu

Tong Yang, Department of Applied Physics, The Hong Kong Polytechnic University, Hung Hom, Kowloon, Hong Kong SAR, the People's Republic of China.
Email: tong-ap.yang@polyu.edu.hk

Andrew T. S. Wee, Department of Physics, National University of Singapore, 2 Science Drive 3, Singapore 117551, Singapore.
Email: phyweets@nus.edu.sg

Funding information
Ministry of Education Singapore, Grant/Award Number: MOE-T2EP50122-0020

Abstract
Metallizing 2D semiconductors is a crucial research area with significant applications, such as reducing the contact resistance at metal/2D semiconductor interfaces. This is a key challenge in the realization of next-generation low-power and high-performance devices. While various methods exist for metallizing Mo- and W-based 2D semiconductors like MoS_2 and WSe_2, effective approaches for Pt-based ones have been lacking. This study demonstrates that platinum dichalcogenides (PtX_2, X = Se or Te) undergo a semiconductor-to-metal transition when grown on niobium dichalcogenides (NbX_2, X = Se or Te). PtX_2/NbX_2 heterostructures were fabricated using molecular beam epitaxy (MBE) and characterized by Raman spectra, scanning transmission electron microscopy (STEM) and scanning tunneling microscopy/spectroscopy (STM/STS). Raman spectra and STEM confirm the growth of 1T-phase PtX_2 and 1H-phase NbX_2. Both 2D STS mapping and layer-dependent STS show that regardless of their layer numbers, both pristine semiconducting $PtSe_2$ and $PtTe_2$ are converted to metallic forms when interfacing with $NbSe_2$ or $NbTe_2$. Density functional theory (DFT) calculations suggest that the metallization of $PtSe_2$ on NbX_2 and $PtTe_2$ on $NbTe_2$ results from interfacial orbital hybridization, while for $PtTe_2$ on $NbSe_2$, it is due to the strong *p*-doping effect caused by interfacial charge transfer. Our work provides an effective method for metallizing PtX_2 semiconductors, which may lead to significant applications such as reducing the contact resistance at metal electrode/2D semiconductor interfaces and developing devices like rectifiers, rectenna, and photodetectors based on 2D Schottky diodes.

KEYWORDS
density functional theory calculations, niobium dichalcogenides, platinum dichalcogenides, scanning tunneling microscopy/spectroscopy, semiconductor-to-metal transition, two-dimensional materials

1 | INTRODUCTION

Metal/semiconductor interface is crucial for both conventional and 2D semiconductor electronics as it plays a vital role in device operations. Metallizing 2D semiconductors is a key research area, with one of its primary applications being the reduction of contact resistance at the metal electrode/2D semiconductor interfaces. This remains a significant challenge in 2D electronics, as achieving Ohmic contact to 2D semiconductors is essential for fully exploiting their potential in device applications.[1] Besides, metallizing 2D semiconductors has other applications, such as 2D Schottky diode-based rectifiers and rectenna.[2–4] Several approaches have been explored to metallize conventional 2D semiconducting transition metal dichalcogenides (TMDs), particularly Mo- and W-based TMDs, including doping,[5–8] phase engineering,[9–16] and hybridization with semimetals like bismuth (Sb) and antimony (Bi).[17–19] However, these approaches often encounter limitations due to a lack of versatility, and the degree of success typically depends on the type of 2D materials. For example, heavy doping is a mature technology in 3D semiconductors, but it is less effective for 2D semiconductors because their atomically thin nature makes it difficult to accommodate dopants. Phase engineering applies only to materials capable of stably existing in both semiconducting and metallic phases, such as 2H/1T-MoS_2 and 2H/1T′-$MoTe_2$.[9–16] Up to now, state-of-the-art technology has successfully metallized MoS_2 by hybridizing it with semimetals such as Sb and Bi, pushing its contact resistance close to the quantum limit.[17,19] Noble transition metal dichalcogenides (NTMDs) are an emerging subclass of TMDs attracting attention due to their unique properties, such as facile synthesis, giant thickness-mediated band gaps, extra-high carrier mobility and conductivity, and robust stability in air. These characteristics position NTMDs as promising materials for applications in electronics and optoelectronics.[20–22] However, effective metallization methods for NTMDs remain much less studied. Hence, developing efficient methods for metallizing NTMDs holds great importance toward enhancing performance levels across devices based on this material class.

Unlike conventional TMDs that can be metallized by microscale phase engineering, PtX_2 predominantly exists stably in the semiconducting 1T phase. This indicates that traditional phase engineering methods are ineffective for PtX_2. Nevertheless, in contrast to conventional TMDs such as MoX_2 and WX_2, NTMDs possess a unique characteristic wherein their electronic properties are highly influenced by interfacial interactions. For instance, due to enhanced interlayer hybridization with increasing layer number, both PtS_2 and $PdSe_2$ exhibit widely tunable bandgaps from ~1.6 and ~1.3 eV for the monolayer to ~0.25 and 0 eV in bulk, respectively,[23–27] while $PtSe_2$ transitions from being a semiconductor with a bandgap of ~2.0 eV to a metal when its thickness exceeds five layers,[28] and $PtTe_2$ even becomes semimetallic starting from its second layer.[29–32] This motivates us to explore an innovative approach to metallize PtX_2 by leveraging the strong interfacial interaction. Specifically, interfacing PtX_2 with other 2D materials that have stronger interactions with them may lead to metallization of PtX_2.[33] This method may offer dual benefits: Firstly, enabling metallization of PtX_2, and secondly, potentially reducing or eliminating the Schottky barrier commonly existing at sharp 2D metal/2D semiconductor interfaces because it does not involve any phase change.

In this article, we demonstrate that platinum dichalcogenides (PtX_2, X = Se or Te) undergo a semiconductor-to-metal transition induced by niobium dichalcogenides (NbX_2, X = Se or Te). High-quality vertical and lateral PtX_2/NbX_2 heterostructures were grown on highly oriented pyrolytic graphite (HOPG) using molecular beam epitaxy (MBE). The structures were studied by Raman spectra, aberration-corrected scanning transmission electron microscopy (STEM) and scanning tunneling microscopy/spectroscopy (STM/STS) as well as density functional theory (DFT) calculations. Raman spectra and STEM confirm the growth of 1T-phase PtX_2 and 1H-phase NbX_2. STM reveals that both $PtSe_2$ and $PtTe_2$ adopt a monolayer-dominated growth mode on NbX_2, whereas $PtSe_2$ forms stacked layers and $PtTe_2$ forms a bilayer film when grown on HOPG. STS results indicate that pristine $PtSe_2$ exhibits a decreasing band gap with an increasing layer number: 2.0 ± 0.1, 1.1 ± 0.1, 0.6 ± 0.1, and 0.20 ± 0.1 eV for 1–4 layers, respectively, and 0 eV for 5 or more layers, while $PtTe_2$ is a semiconductor with a bandgap of ~0.8 eV in monolayer form and becomes a semimetal from the second layer onwards. Both $PtSe_2$ and $PtTe_2$ are converted to metallic when interfacing with $NbSe_2$ and $NbTe_2$. Such semiconductor-to-metal transition occurs not only in monolayer PtX_2 directly in contact with NbX_2, but also in multilayer PtX_2 regardless of their layer numbers. DFT calculations suggest that the metallization of $PtSe_2$ on NbX_2 and $PtTe_2$ on $NbTe_2$ results from interfacial orbital hybridization, while for $PtTe_2$ on $NbSe_2$ it is due to the strong *p*-doping effect caused by interfacial charge transfer. This work provides an effective strategy for metallizing NTMDs and offers a deep insight into the metallization at an atomic level, which may lead to significant applications such as reducing contact resistance at metal electrode/2D semiconductor interfaces and developing devices like rectifiers, rectenna, and photodetectors based on 2D Schottky diodes.

2 | RESULTS AND DISCUSSION

Based on previous research, both $PtSe_2$ and $PtTe_2$ crystallize in an octahedral (1T) structure with $P3\overline{m}1$ space group (Figure 1A) within a growth or annealing temperature range of 200–300°C, while above this range, they lose some chalcogen atoms and transform into other Pt-chalcogenides with lower chalcogen stoichiometries than the PtX_2.[30,34–38] For $NbSe_2$, growth occurs at temperatures <400°C for the trigonal prismatic (1H) phase with $P63/mmc$ space group (Figure 1B), between 400 and 500°C for the mixed 1T and 1H phases, and >500°C for the 1T phase.[39–42] Therefore, to avoid complications arising from mixing different crystal phases or phase transitions due to temperature change, we selected 280°C as the growth temperature for both PtX_2 and NbX_2. While prior reports indicated $NbTe_2$ to be in the 1T phase,[43–45] it was found that it crystallizes in the 1H phase in our experiment, as will be discussed later. This finding is supported by a very recent work, which provides strong evidences for the existence of incognizant H phase in monolayer $NbTe_2$ and suggests the preferred growth of H phase at low growth temperatures.[46] Vertical and lateral heterostructures were prepared by sequential growths of NbX_2 and PtX_2, as schematized in Figure 1C: NbX_2 was firstly grown by co-deposition of Nb and Se or Te onto HOPG at 280°C, then followed by the growth of PtX_2 by co-deposition of Pt and Se or Te atoms onto the NbX_2/HOPG at 280°C. By adjusting the amounts of each material to submonolayer levels, both lateral (Figure 1D) and vertical (Figure 1E) heterostructures were achieved for STEM and STM/STS analyses. For clearance and simplicity, we refer to the n-layer as nL (where $n = 1, 2, 3, \ldots$), the lateral heterostructure of 1L-PtX_2/1L-NbX_2 as 1L-PtX_2–1L-NbX_2, and the vertical heterostructure of 1L-PtX_2/1L-NbX_2 as 1L-PtX_2⊥1L-NbX_2 hereafter. When there is no need to distinguish between lateral and vertical heterostructures, we still use PtX_2/NbX_2 to refer to heterostructures. In certain vertical heterostructures, the second layer of PtX_2 extends over the 1L-PtX_2–1L-NbX_2 below as schematized in Figure 1E, providing an intuitive comparison of the influence of 1L-PtX_2 and 1L-NbX_2 on the electronic properties of the upper PtX_2 layer.

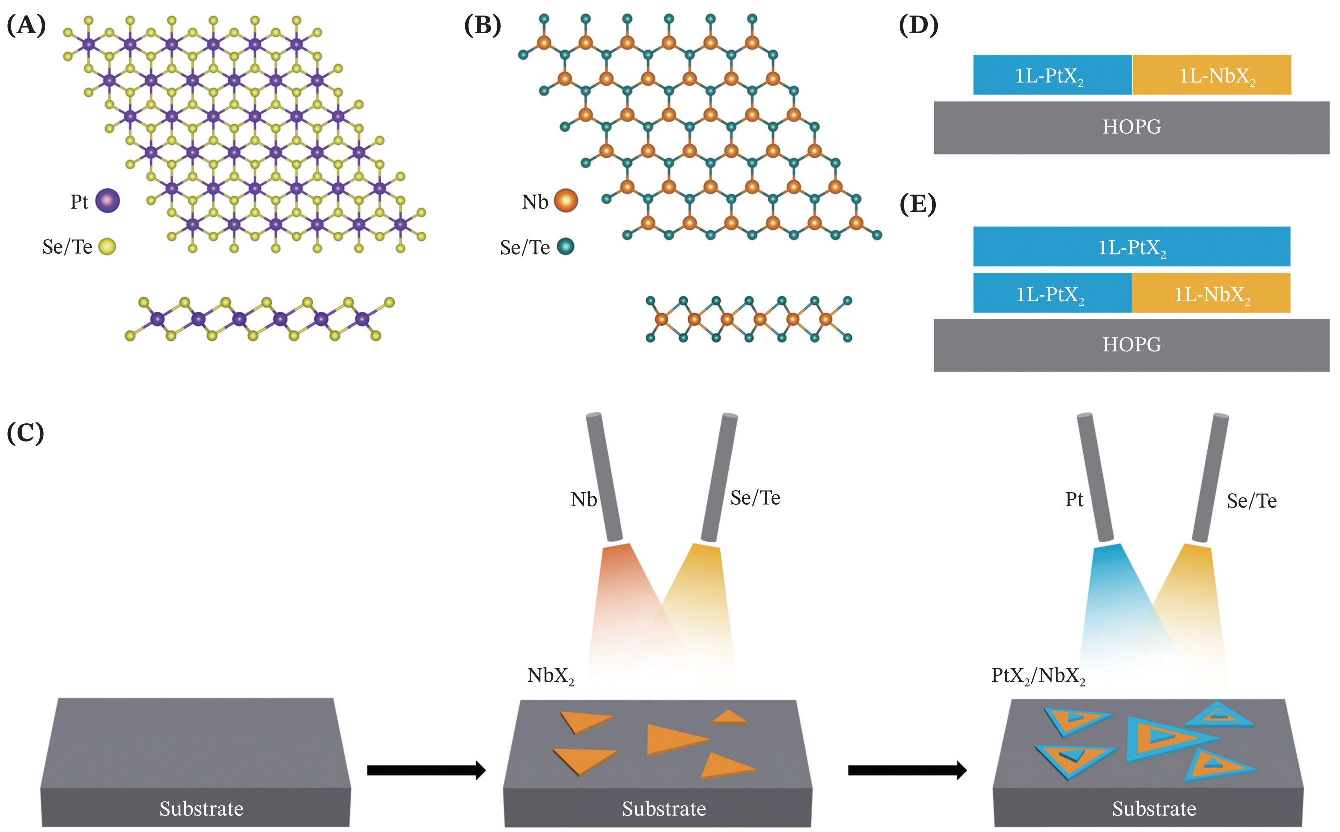

FIGURE 1 (A) and (B) Lattice structures of 1T-phase PtX_2 and 1H-phase NbX_2, respectively. (C) Schematic of sample preparation: NbX_2 is first grown on HOPG substrate, then PtX_2 is grown, forming lateral and vertical heterostructures. (D) Schematic of a lateral heterostructure. (E) Schematic of a vertical heterostructure, in which the upper PtX_2 layer extends over the 1L-PtX_2–1L-NbX_2 lateral heterostructure below.

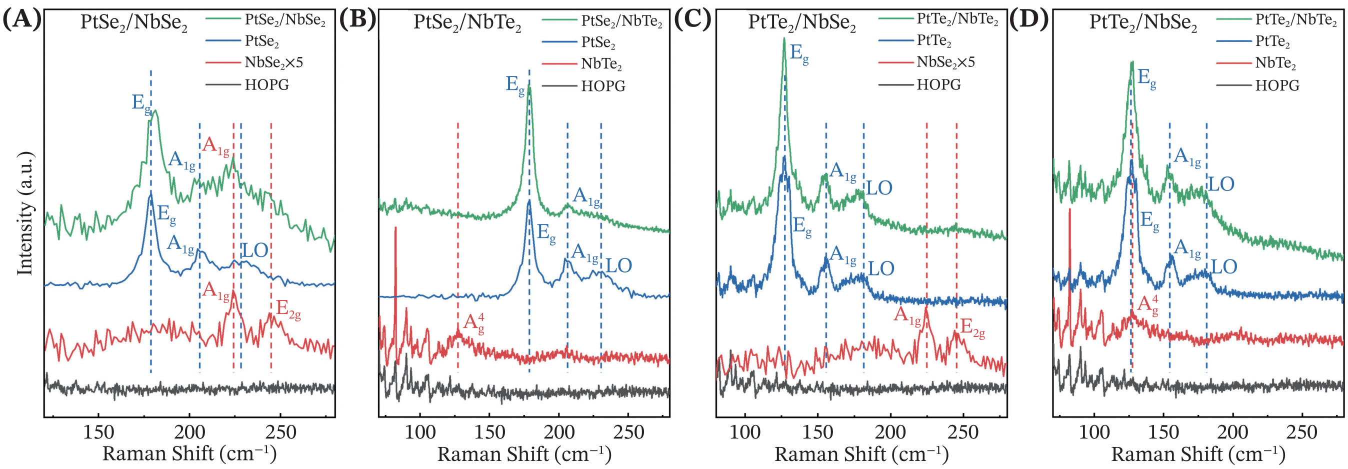

FIGURE 2 Raman spectra. (A)–(D) Raman spectra of 1L-$PtSe_2$⊥1L-$NbSe_2$, 1L-$PtSe_2$⊥1L-$NbTe_2$, 1L-$PtTe_2$⊥1L-$NbSe_2$, and 1L-$PtTe_2$⊥1L-$NbTe_2$, respectively. In each panel, Raman spectra of PtX_2, NbX_2, and HOPG were added as a comparison.

The growth of NbX_2 and PtX_2 as well as PtX_2/NbX_2 heterostructures was first monitored using Raman spectra (Figure 2). To simplify the analysis, we just focus on 1L-PtX_2⊥1L-NbX_2 to disregard the influence of 1L-PtX_2–1L-NbX_2. This is feasible because NbX_2 predominantly forms monolayer films on HOPG, while PtX_2 does so on NbX_2/HOPG, as confirmed by STM later (Figure 5). By maintaining constant growth conditions (such as temperature and evaporation rates of metals and chalcogens), the thickness in unit of layer is directly proportional to the growth time when the thickness is ≤1L. Therefore, by controlling the growth time, 1L-PtX_2⊥1L-NbX_2 with minimal 1L-PtX_2–1L-NbX_2 can be obtained. In the case of $NbSe_2$ (Figure 2A,C), peaks at 224.8 and 243.5 cm^{-1} correspond to the A_{1g} and E_{2g} vibrational modes of $NbSe_2$.[47–49] For $NbTe_2$ (Figure 2B,D), only a peak at ∼127 cm^{-1} can be barely observed, which should represent the A_g^4 vibrational mode of $NbTe_2$.[50–52] The Raman signals for both $NbSe_2$ and $NbTe_2$ are extremely weak due to their monolayer thickness and being the bottom layer. This is consistent with previous studies.[47–49,51] In $PtSe_2$, three peaks are clearly identified at ∼178.0, 205.8 and 229.7 cm^{-1}, corresponding to the E_g, A_{1g} and longitudinal optical (LO) modes of $PtSe_2$, respectively.[53,54] Regarding $PtTe_2$, the E_g, A_{1g} and LO Raman active modes are observed at ∼126.6, 155 and 179 cm^{-1}, respectively, in line with previous reports.[55,56] These Raman spectra confirm the growth of PtX_2 and NbX_2. Due to the extremely weak Raman signals from NbX_2 and partial overlap with the peaks of PtX_2 (Figure 2A,D), only the Raman peaks of PtX_2 can be observed in the 1L-PtX_2⊥1L-NbX_2 heterostructures. The Raman features of both $PtSe_2$ and $PtTe_2$ remain unchanged in all 1L-PtX_2⊥1L-NbX_2 heterostructures, suggesting that no phase change of PtX_2 occurs when grown on NbX_2.

During the preparation of heterostructures using the MBE method, alloying or doping may occur. Therefore, STEM was conducted to further study the microstructures of PtX_2/NbX_2 heterostructures, as shown in Figure 3. Lateral PtX_2/NbX_2 boundaries are indicated by white dashed lines. In the case of $PtSe_2/NbSe_2$ (Figure 3A), the boundaries appear somewhat disordered due to atom interdiffusion from PtX_2 and NbX_2, but this disorder is confined to a few nanometers near the boundaries. Away from the boundaries, clear lattice structures are observed: 1H-$NbSe_2$ with a lattice constant of ∼0.35 nm and 1T-$PtSe_2$ with a lattice constant of ∼0.37 nm, as shown in Figure 3B,C, respectively. In contrast, for $PtSe_2/NbTe_2$, sharper boundaries are observed. However, there are point defects present in $NbTe_2$ regions arranged in straight lines at angles of approximately 60° between different lines (indicated by yellow lines in Figure 3D). Since during the growth of $PtSe_2$, previously grown $NbTe_2$ would be inevitably exposed to Se, these defects are speculated to be Se atoms introduced during $PtSe_2$ growth. To prove this, we used XPS to investigate how Se affects $NbTe_2$ by subjecting $NbTe_2$ to the same Se atmosphere as in $PtSe_2$ growth at 280°C. The results are presented in Figure S1 of the Supporting Information. With the increase of exposure time of $NbTe_2$ in the Se atmosphere, the peak intensity of Te3*d* gradually decreases, while that of Se3*d* gradually increases, showing the partial replacement of Te atoms by Se atoms. Despite these defects, the zoom-in image verifies the 1H phase of $NbTe_2$ with a lattice constant of ∼0.37 nm (Figure 3E), while the $PtSe_2$ regions show the 1T phase with a lattice constant of ∼0.37 nm (Figure 3F). The

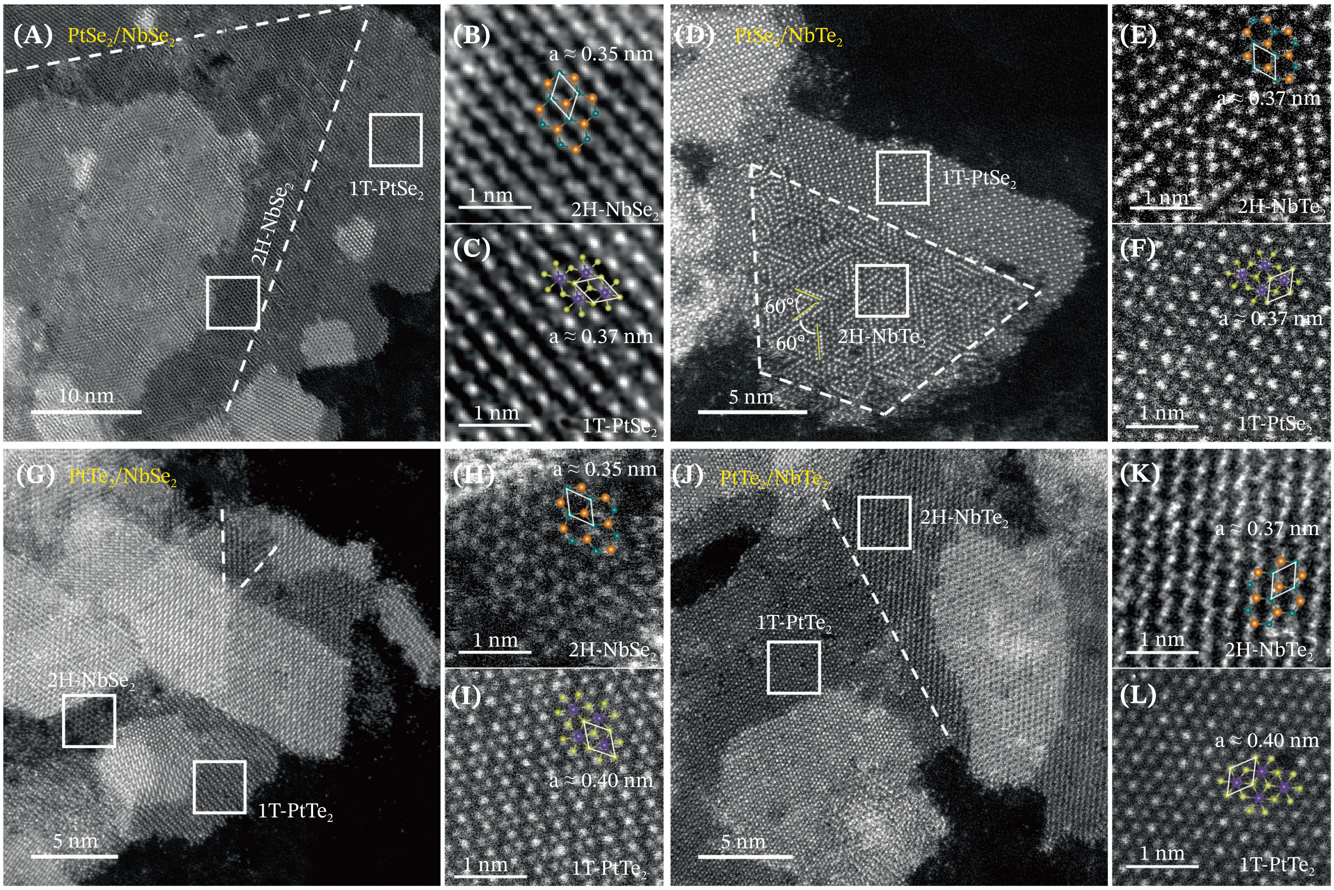

FIGURE 3 STEM images of PtX_2/NbX_2 heterostructures. Large-scale and zoom-in images of (A)–(C) $PtSe_2/NbSe_2$, (D)–(F) $PtSe_2/NbTe_2$, (G)–(I) $PtTe_2/NbSe_2$, and (J)–(L) $PtTe_2/NbTe_2$. PtX_2/NbX_2 boundaries are indicated by white dashed lines. The zoom-in images are from the areas enclosed by white squares in the corresponding large-scale images and are overlaid with lattice models and lattice constants to show the 1T phase of PtX_2 and 1H phase of NbX_2. In panel D, the directions of typical lines of defects are indicated by yellow lines and they form ~60° angles. There is no apparent alloying occurring in heterostructures other than the $NbTe_2$ within the $PtSe_2/NbTe_2$ heterostructure.

sharpest boundaries were found in $PtTe_2/NbSe_2$ and $PtTe_2/NbTe_2$ heterostructures (Figure 3G–L), where distinct phases were identified through zoom-in images with their respective lattice constants confirmed: For example, the $NbSe_2$ region (Figure 3H) shows 1H phase with a lattice constant of ~0.35 nm, the $NbTe_2$ region (Figure 3K) shows 1H phase with a lattice constant of ~0.37 nm, and the $PtTe_2$ regions (Figure 3I,L) show 1T phase with a lattice constant of ~0.40 nm. Overall findings from STEM analyses confirm the 1T phase of PtX_2 and 1H phase of NbX_2 and support that there is no apparent alloying occurring in heterostructures other than the $NbTe_2$ within the $PtSe_2/NbTe_2$ heterostructure.

The impact of NbX_2 on the electronic properties of PtX_2 was examined using STM/STS. Initially, we analyzed the morphological and electronic properties of pristine NbX_2 and PtX_2 on HOPG, as depicted in Figure 4. Both $NbSe_2$ and $NbTe_2$ form crystal islands at almost monolayer on HOPG with their first layers being ~0.85 and ~1.0 nm in apparent height, respectively (Figure 4A,B). The atomic resolution STM (AR-STM) images show their good crystallinity with lattice constants of ~0.35 and ~0.37 nm, respectively (Figure 4E,F). The gapless STS confirms their metallic nature (Figure 4I,J), consistent with previous reports.[39,57] Unlike NbX_2, $PtSe_2$ forms a stack of different layers with its first layer and second layer being ~0.70 and ~0.60 nm in apparent height, respectively (Figure 4C), while $PtTe_2$ prefers bilayer growth mode with its first layer and second layer being ~0.90 and ~0.50 nm, respectively (Figure 4D). The AR-STM images validate their excellent crystallinity with lattice constants of ~0.37 and ~0.40 nm for $PtSe_2$ and $PtTe_2$, respectively (Figure 4G,H). The lattice constants of PtX_2 and NbX_2 obtained through STM match well with those by STEM in the previous section. The STS of $PtSe_2$ shows a layer-dependent bandgap of ~2.0, ~1.1, ~0.6, and ~0.2 eV for layer numbers from 1 to 4 (Figure 4K), while for $PtTe_2$ it shows a bandgap of ~0.8 eV for the monolayer and 0 eV for the bilayer. The layer-dependent bandgaps of $PtSe_2$

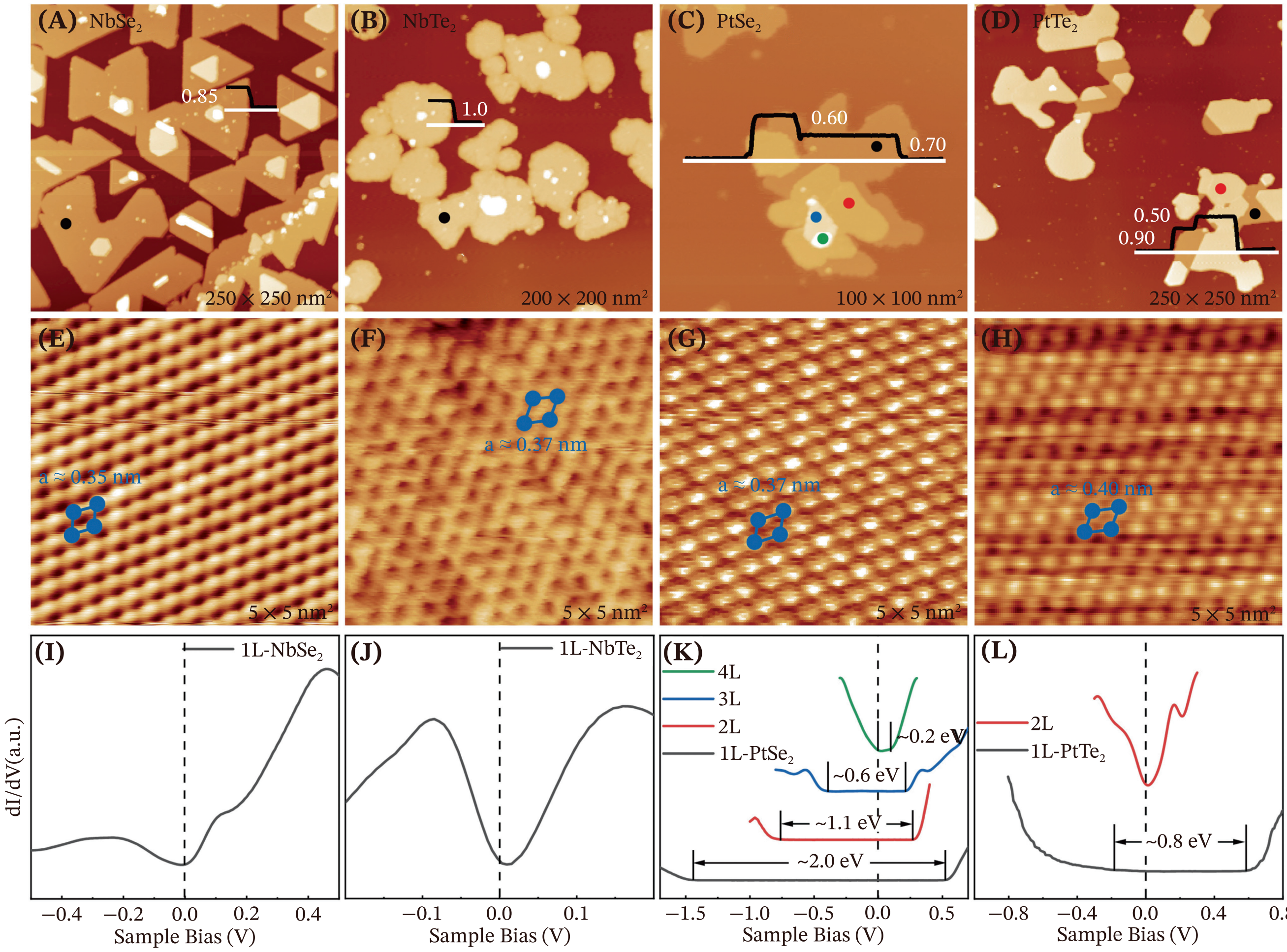

FIGURE 4 STM/STS of pristine NbX_2/HOPG and PtX_2/HOPG. (A)–(D) Large-scale STM images of $NbSe_2$, $NbTe_2$, $PtSe_2$, and $PtTe_2$, respectively. Height profiles along the white lines in each panel are included to display their apparent heights (unit: nm). (E)–(H) The corresponding atomic-resolution STM images with unit cell and lattice constants shown. (I)–(L) The corresponding STS taken at the colored dots in the large-scale images. (A)–(D) $V_{sample} = -2.0$ V, $I = 5$ pA. (E)–(H) $V_{sample} = 0.01$ V, $I = 400$ pA. (I) and (J) $V_{sample} = 0.5$ V, $I = 250$ pA. (K) and (L) $V_{sample} = 1.0$ V, $I = 250$ pA.

and $PtTe_2$ are consistent with our previous studies and literatures,[28,31,32] proving their good crystallinity and semiconducting behavior.

Figure 5A–D present the STM morphologies of PtX_2/NbX_2 heterostructures and Figure 5E–H are the corresponding zoom-in images. From an overall perspective, there are two prominent features: One is that PtX_2 mainly grows along the edge of NbX_2 islands, forming 1L-PtX_2–1L-NbX_2, and on top of NbX_2 islands, forming 1L-PtX_2⊥1L-NbX_2; The other one is that PtX_2 forms monolayer-dominated films on NbX_2, which are distinguished from their pristine growth behaviors on HOPG, indicating a stronger van der Waals (vdW) interaction between PtX_2 and NbX_2. As materials tend to grow where they experience stronger interactions, locations with stronger interactions will have more materials growing there, while locations with weaker interactions will have fewer materials growing in that area. In order to qualitatively determine the ranking of vdW interactions in the 1L-PtX_2⊥1L-NbX_2, we calculated the ratio of the area where a single layer of PtX_2 grows on top of another single layer of PtX_2 (i.e., 2L-PtX_2) and where a single layer of PtX_2 grows on top of a single layer of NbX_2 (i.e., 1L-PtX_2⊥1L-NbX_2) (Figure S2), and the results are shown in Table S1. The results show that the ranking of the vdW interactions is $PtSe_2$/$NbTe_2$ > $PtSe_2$/$NbSe_2$ > $PtSe_2$/$PtSe_2$ ≈ $PtSe_2$/HOPG for $PtSe_2$ and $PtTe_2$/$NbTe_2$ > $PtTe_2$/$NbSe_2$ ≈ $PtTe_2$/$PtTe_2$ > $PtTe_2$/HOPG for $PtTe_2$. In Figure 5E–H, boundaries between PtX_2 and NbX_2 (indicated by white dashed lines) are visible but vary in sharpness. For $PtSe_2$/$NbSe_2$ (Figure 5E), the boundaries are less distinct due to the interdiffusion of atoms at the interface, as shown in our STEM study (Figure 3). In Figure 5F, the color, which represents the apparent

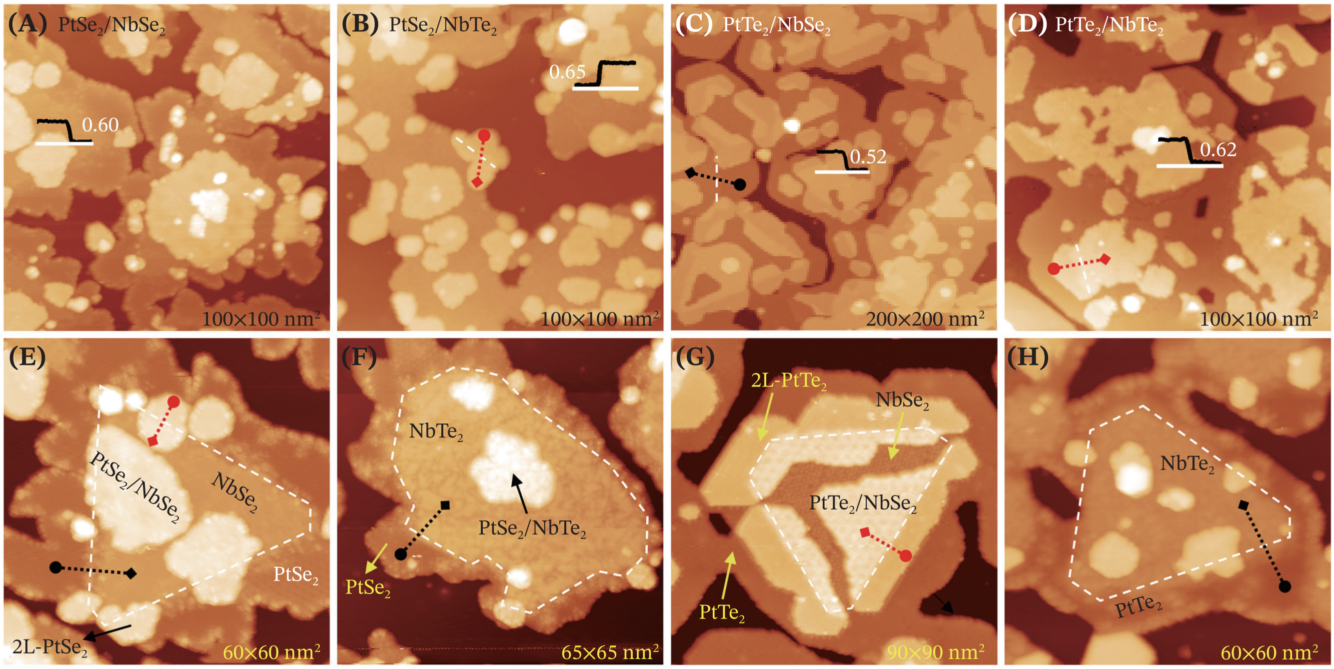

FIGURE 5 STM of PtX_2/NbX_2 heterostructures. (A)–(D) Large-scale STM images of $PtSe_2/NbSe_2$, $PtSe_2/NbTe_2$, $PtTe_2/NbSe_2$, $PtTe_2/NbTe_2$ heterostructures, respectively. Height profiles along the white lines in each panel are included to display the apparent height of 1L-PtX_2 grown on 1L-NbX_2 (unit: nm). (E)–(H) The corresponding zoom-in images, respectively. White dashed lines indicate the boundaries between 1L-PtX_2 and 1L-NbX_2. (A)–(D) $V_{sample} = -2.0$ V, $I = 5$ pA. (E)–(H) $V_{sample} = -1.0$ V, $I = 20$ pA.

height, of the $NbTe_2$ region is obviously non-uniform. This is because some of the Te atoms were replaced by Se atoms during the growth of $PtSe_2$, altering surface electronic states, as discussed earlier. The sharpest boundaries appear between $PtTe_2$ and $NbSe_2$ (Figure 5G). Owing to the strong interaction between $NbSe_2$ and $PtTe_2$, a clear contrast can be seen in the second-layer $PtTe_2$ extending over the 1L-$PtTe_2$–1L-$NbSe_2$ below. For $PtTe_2/NbTe_2$ (Figure 5H), although the boundaries are sharp as revealed by STEM (Figure 3), the contrast of surface electronic states across the boundaries is much more blurred than for $PtTe_2/NbSe_2$, which means that the influence of the boundaries on the electronic states of these two materials extends over a longer distance. The apparent height of 1L-PtX_2 grown on 1L-NbX_2 was measured to be ∼0.60 nm and ∼0.65 nm for $PtSe_2$ on $NbSe_2$ and $NbTe_2$, respectively, and ∼0.52 nm and ∼0.62 nm for $PtTe_2$ on $NbSe_2$ and $NbTe_2$, respectively, as shown by the height profiles in Figure 5A–D. These apparent heights are apparently smaller than those of 1L-PtX_2 directly grown on HOPG (Figure 4A–D), further implying a stronger interaction between PtX_2 and NbX_2.

To investigate the electronic evolution in lateral PtX_2/NbX_2 heterostructures, we conducted position-dependent STS along the black dashed arrows from the PtX_2 region (round dot) to the NbX_2 region (square dot) in Figure 5 and presented the findings in Figure 6. The upper panels of Figure 6 display 2D STS mappings from 1L-PtX_2 to 1L-NbX_2, while the lower panels show typical STS spectra corresponding to the dots in the upper panels with red dots in the 1L-PtX_2 region, green dots in the boundary region, and blue dots in the 1L-NbX_2 region. In the case of 1L-$PtSe_2$/1L-$NbSe_2$ (Figure 6A,E), there is a consistent bandgap value of ∼2.0 eV observed within the area of 1L-$PtSe_2$, aligning with that of pristine 1T-$PtSe_2$ on HOPG, confirming its pure phase. Changes are confined to a narrow zone near boundaries. Repeatable STS measurements in the $NbSe_2$ region confirm the pure phase of $NbSe_2$. For $PtSe_2/NbTe_2$ (Figure 6B,F), a constant bandgap of ∼2.0 eV is also maintained within the $PtSe_2$ region, indicating its purity as seen with pristine $PtSe_2$ on HOPG. In the $NbTe_2$ region, metallic properties are confirmed; however, relatively random STS spectra are observed due to the partial replacement of Te by Se, as revealed by STEM (Figure 3B) and XPS (Figure S1). Regarding $PtTe_2/NbSe_2$ and $PtTe_2/NbTe_2$, STS shows a consistent bandgap of ∼0.8 eV in the $PtTe_2$ region and good repeatability of metallic character in the $NbSe_2$ and $NbTe_2$ regions, confirming their purity. The difference between these two heterostructures is that in $PtTe_2/NbSe_2$, the change occurs sharply within a very narrow region at the boundaries due to the sharp boundaries between $PtTe_2$ and $NbSe_2$, while in $PtTe_2/NbTe_2$, the change is relatively slower at the

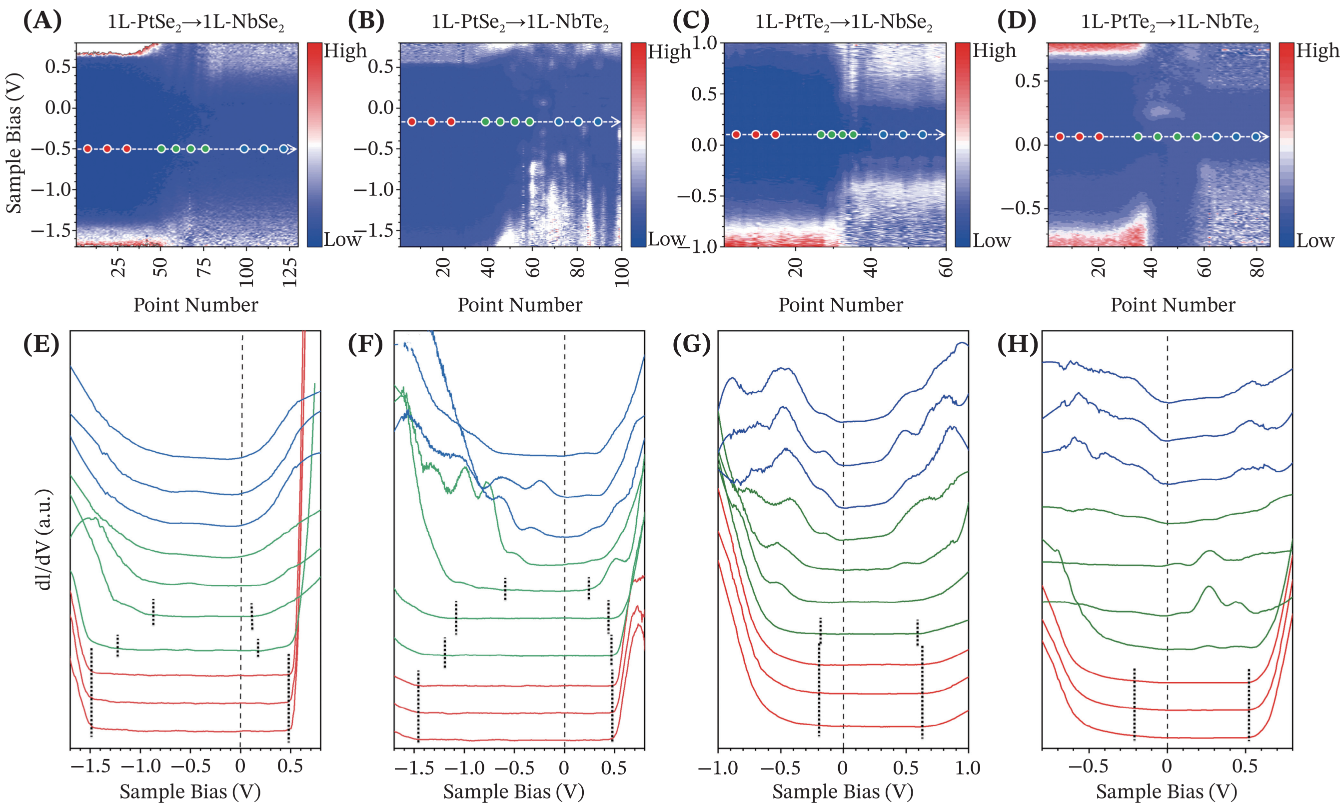

FIGURE 6 STS evolution from 1L-PtX$_2$ to 1L-NbX$_2$. (A)–(D) upper panels: 2D STS mapping from 1L-PtSe$_2$ to 1L-NbSe$_2$, 1L-PtSe$_2$ to 1L-NbTe$_2$, 1L-PtTe$_2$ to 1L-NbSe$_2$, and 1L-PtTe$_2$ to 1L-NbTe$_2$, respectively. Lower panels: Selected STS corresponding to the red, green and blue dots in upper panels. Short dashed lines indicate the band edges. (A)–(H) $V_{sample} = 1.0$ V, $I = 250$ pA.

boundaries because the influence of the boundaries on the electronic states of these two materials extends over a longer distance.

In certain vertical heterostructures, the second layer of PtX$_2$ extends over the underlying 1L-PtX$_2$–1L-NbX$_2$, as schematized in Figure 1E. This allows for a direct comparison of the impact of the lower PtX$_2$ layer and NbX$_2$ layer on the electronic properties of the upper PtX$_2$ layer by comparing the STS of 1L-PtX$_2$⊥1L-NbX$_2$ with that of 1L-PtX$_2$⊥1L-PtX$_2$ (i.e., 2L-PtX$_2$) through 2D STS mapping, as illustrated in Figure 7. The upper panels of Figure 7 display the 2D STS mappings from 2L-PtX$_2$ to 1L-PtX$_2$⊥1L-NbX$_2$, while the lower panels show typical STS spectra corresponding to the dots in the upper panels with red dots in the 2L-PtX$_2$ region, green dots in the boundary region, and blue dots in the 1L-PtX$_2$⊥1L-NbX$_2$ region. For PtSe$_2$/NbSe$_2$ (Figure 7A,E), along the scanning path from 2L-PtSe$_2$ to 1L-PtSe$_2$⊥1L-NbSe$_2$, there is initially a constant bandgap of ~1.1 eV in the 2L-PtSe$_2$ region, which then rapidly narrows upon approaching the underlying 1L-PtSe$_2$–1L-NbSe$_2$ boundary before completely disappearing within the 1L-PtSe$_2$⊥1L-NbSe$_2$ area. This not only indicates the pure phase of PtSe$_2$ but also showcases its semiconductor-to-metal transition when interfacing with NbSe$_2$. For PtSe$_2$/NbTe$_2$ (Figure 7B,F), the bandgap also remains constant in the 2L-PtSe$_2$ region, then rapidly narrows near the underneath 1L-PtSe$_2$–1L-NbTe$_2$ boundary and ultimately disappears in the 1L-PtSe$_2$⊥1L-NbTe$_2$ region. However, the STS appears relatively chaotic in the 1L-PtSe$_2$⊥1L-NbTe$_2$ region, likely due to the random electronic states of the underlying 1L-NbTe$_2$ caused by the partial replacement of Te by Se, as discussed before. In PtTe$_2$/NbSe$_2$ (Figure 7C,G) and PtTe$_2$/NbTe$_2$ (Figure 7D,H) heterostructures, the STS reveals sharp evolutions at the boundaries from 2L-PtTe$_2$ to 1L-PtTe$_2$⊥1L-NbX$_2$. However, no bandgap is observed in the 1L-PtTe$_2$⊥1L-NbX$_2$ region, indicating a semiconductor-to-metal transition of 1L-PtTe$_2$ on NbX$_2$. In pristine 2L-PtTe$_2$ (i.e., 1L-PtTe$_2$⊥1L-PtTe$_2$), the density of states (DOS) above the Fermi level (positive sample bias) is higher in intensity than that below the Fermi level (negative sample bias). Notably, for both 1L-PtTe$_2$⊥1L-NbSe$_2$ and 1L-PtTe$_2$⊥1L-NbTe$_2$, there is a reversal where the DOS below the Fermi level becomes larger than that above the Fermi level.

To illustrate the difference in conductivities between PtX$_2$ on HOPG and on NbX$_2$, typical spectra of tunneling

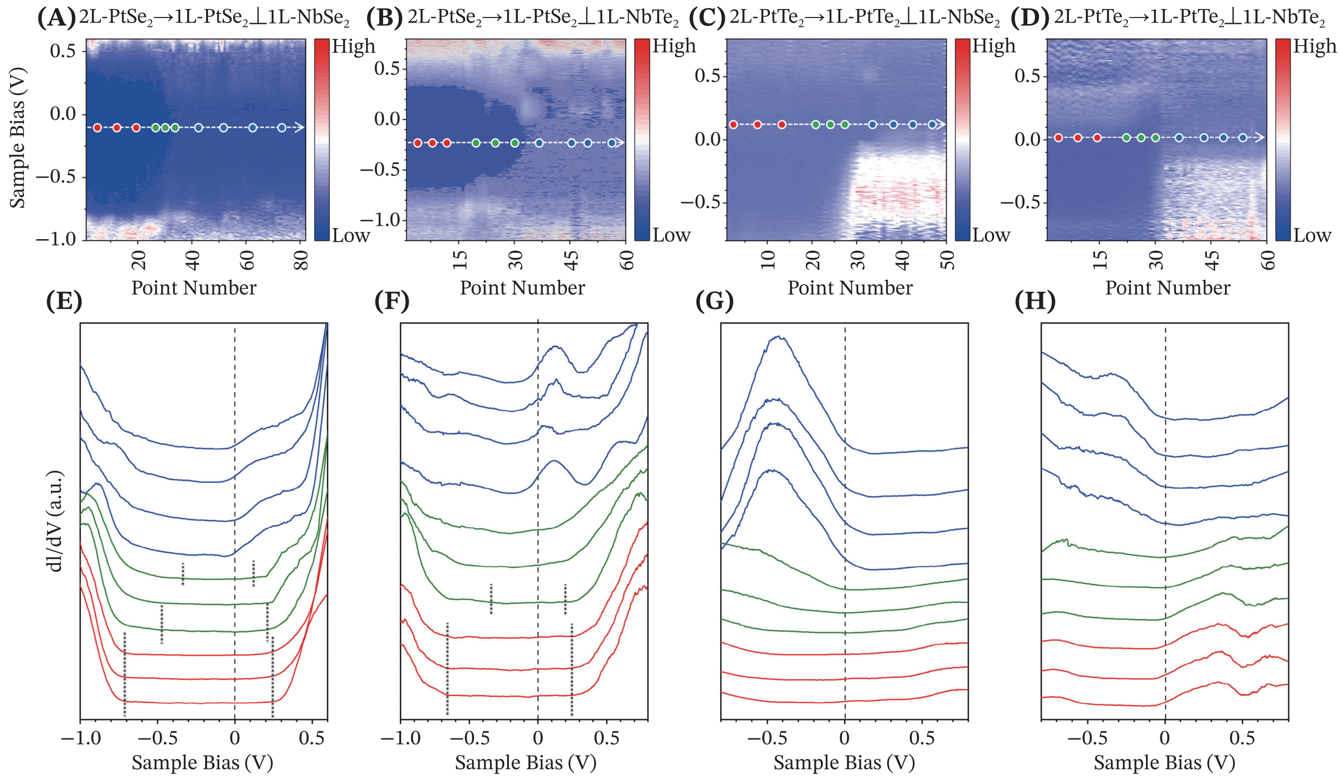

FIGURE 7 STS evolution from 2L-PtX_2 to 1L-PtX_2⊥1L-NbX_2. (A)–(D) 2D STS mappings from 2L-$PtSe_2$ to 1L-$PtSe_2$⊥1L-$NbSe_2$, 2L-$PtSe_2$ to 1L-$PtSe_2$⊥1L-$NbTe_2$, 2L-$PtTe_2$ to 1L-$PtTe_2$⊥1L-$NbSe_2$, and 2L-$PtTe_2$ to 1L-$PtTe_2$⊥1L-$NbTe_2$, respectively. (E)–(H) The corresponding STS of the red, green and blue dots in upper panel (A)–(D). Short dashed lines indicate the band edges. (A)–(H) $V_{sample} = 1.0$ V, $I = 250$ pA.

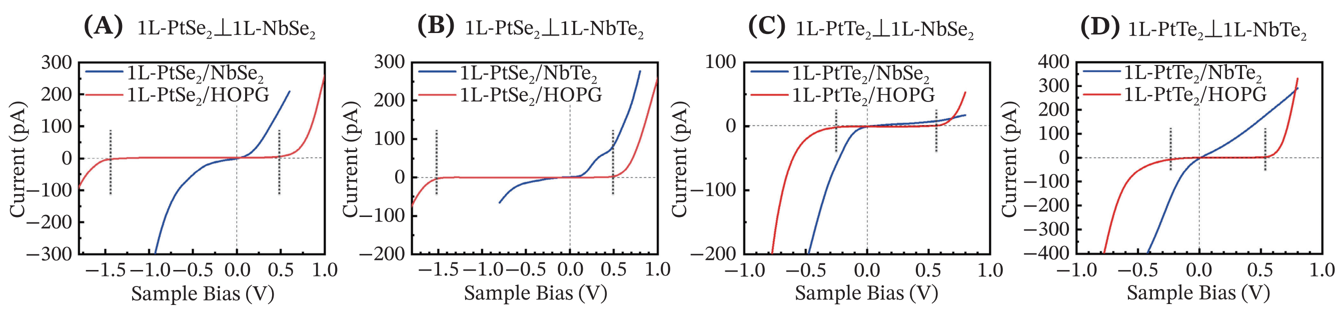

FIGURE 8 Tunneling current vs sample bias spectra of (A) 1L-$PtSe_2$⊥1L-$NbSe_2$ and 1L-$PtSe_2$/HOPG, (B) 1L-$PtSe_2$⊥1L-$NbTe_2$ and 1L-$PtSe_2$/HOPG, (C) 1L-$PtTe_2$⊥1L-$NbSe_2$ and 1L-$PtTe_2$/HOPG, and (D) 1L-$PtTe_2$⊥1L-$NbTe_2$ and 1L-$PtTe_2$/HOPG. Short dashed lines indicate the band edges. (A)–(D) $V_{sample} = 1.0$ V, $I = 250$ pA.

current versus sample bias are plotted, as depicted in Figure 8. In the case of 1L-$PtSe_2$/HOPG, the tunneling current remains close to zero within a sample bias range from approximately −1.4 to 0.6 V, consistent with its bandgap of around 2.0 eV. Conversely, for 1L-$PtSe_2$⊥1L-$NbSe_2$ and 1L-$PtSe_2$⊥1L-$NbTe_2$, the tunneling currents deviate significantly from zero when the samples bias is non-zero, indicating the metallic nature of 1L-$PtSe_2$ on NbX_2 (see Figure 8A,B). Similarly, for 1L-$PtTe_2$/HOPG, there is nearly no tunneling current observed within a sample bias spanning roughly −0.2 to 0.6 V corresponding to its bandgap of about 0.8 eV. However, both 1L-$PtTe_2$⊥1L-$NbSe_2$ and 1L-$PtTe_2$⊥1L-$NbTe_2$ demonstrate non-zero tunneling currents under non-zero sample bias, signifying a semiconductor-to-metal transition of $PtTe_2$ induced by NbX_2, as shown in Figure 8C,D. To further confirm if the transition only occurs in the PtX_2 layer directly in contact with NbX_2, we measured the layer-dependent STS of PtX_2 on NbX_2 and show the results in Figure 9. It can be seen that both $PtSe_2$ and

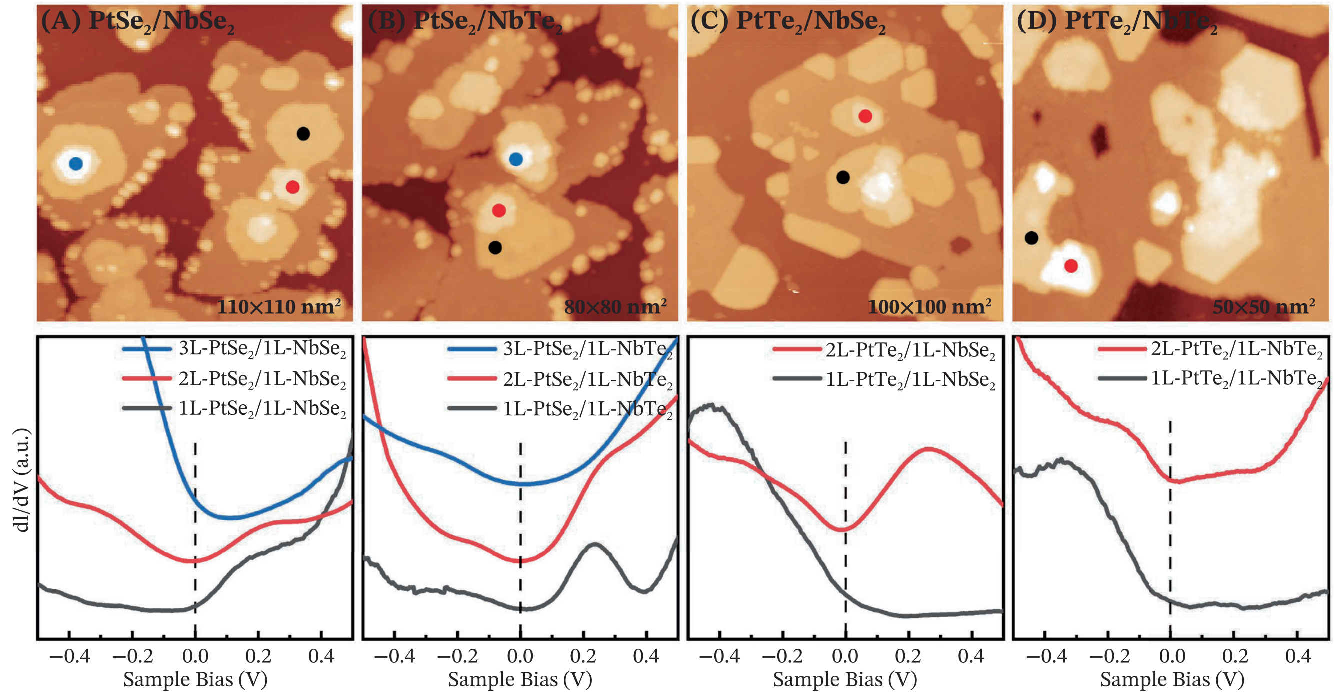

FIGURE 9 Layer-dependent STS of (A) $PtSe_2 \perp 1L\text{-}NbSe_2$, (B) $PtSe_2 \perp 1L\text{-}NbTe_2$, (C) $PtTe_2 \perp 1L\text{-}NbSe_2$, and (D) $PtTe_2 \perp 1L\text{-}NbTe_2$. The upper panels display the STM images, and the lower panels present the layer-dependent STS corresponding to the dots in the upper panels. The Black dots are on the 1L-PtX_2/1L-NbX_2, red dots on the 2L-PtX_2/1L-NbX_2, and blue dots on the 3L-PtX_2/1L-NbX_2. Both $PtSe_2$ and $PtTe_2$ exhibit metallic properties on NbX_2 regardless of their layer numbers. (A)–(D) STM images: $V_{sample} = -2.0$ V, $I = 5$ pA. (A)–(D) STS: $V_{sample} = 1.0$ V, $I = 250$ pA.

TABLE 1 Layer-dependent bandgaps of PtX_2 on NbX_2 and HOPG.

Substrates / PtX_2	$NbSe_2$	$NbTe_2$	HOPG	
$PtSe_2$	Metallic	Metallic	1L	2.0 ± 0.1 eV
			2L	1.1 ± 0.1 eV
			3L	0.6 ± 0.1 eV
			4L	0.2 ± 0.1 eV
			≥5L	0 eV
$PtTe_2$	Metallic	Metallic	1L	0.8 ± 0.1 eV
			≥2L	0 eV

$PtTe_2$ exhibit metallic properties on NbX_2 regardless of their layer numbers. The layer-dependent bandgaps of PtX_2 on NbX_2 and HOPG are summarized in Table 1.

DFT calculations were performed to shed light on the semiconductor-to-metal transition of 1T-PtX_2 when interfacing with 1H-NbX_2. The optimized in-plane lattice constant is 3.732 Å for 1T-$PtSe_2$, 4.003 Å for 1T-$PtTe_2$, 3.476 Å for 1H-$NbSe_2$, and 3.699 Å for 1H-$NbTe_2$, which are close to our experimental values. Following Anderson's rule, the energy levels of isolated 1T-PtX_2 were first aligned with those of isolated 1H-NbX_2 (refer to Figure S3). The Fermi level of 1H-NbX_2 is situated within the band gap of 1T-$PtSe_2$, indicative of weak charge transfer between them. On the contrary, the Fermi levels of 1H-$NbSe_2$ and 1H-$NbTe_2$ are respectively 0.631 eV (0.717 eV) and 0.178 eV (0.132 eV) below the valence band maximum of 1T-$PtTe_2$ at the optB88-vdW (HSE06) level of theory, suggesting that interfacial charge transfer from 1T-$PtTe_2$ to 1H-NbX_2 may play an important role in the semiconductor-to-metal transition of 1T-$PtTe_2$, especially for the 1T-$PtTe_2 \perp$1H-$NbSe_2$ heterostructure. Figure 10 shows the calculated projected band structures of the 1T-$PtX_2 \perp$1H-NbX_2 heterostructures in their respective most stable stacking configurations (see Figures S4–S7). For 1T-$PtTe_2 \perp$1H-$NbSe_2$ in Figure 10C, the strong interfacial charge transfer leads to pronounced *p*-doping of 1T-$PtTe_2$. This is consistent with our experimental observations that there are more states below the Fermi level than above the Fermi level. When interfacing with 1H-$NbTe_2$, however, *p*-doping of 1T-$PtTe_2$ is weaker due to a smaller offset (0.178 eV) (Figure 10D). For 1T-$PtSe_2 \perp$1H-NbX_2 heterostructures (Figure 10A,B), the interfacial orbital hybridization is likely responsible for the experimentally observed semiconductor-to-metal transition. The 1H-NbX_2 stacking-induced metallicity of 1T-PtX_2 was further revealed by the projection ratio of 1T-PtX_2 to

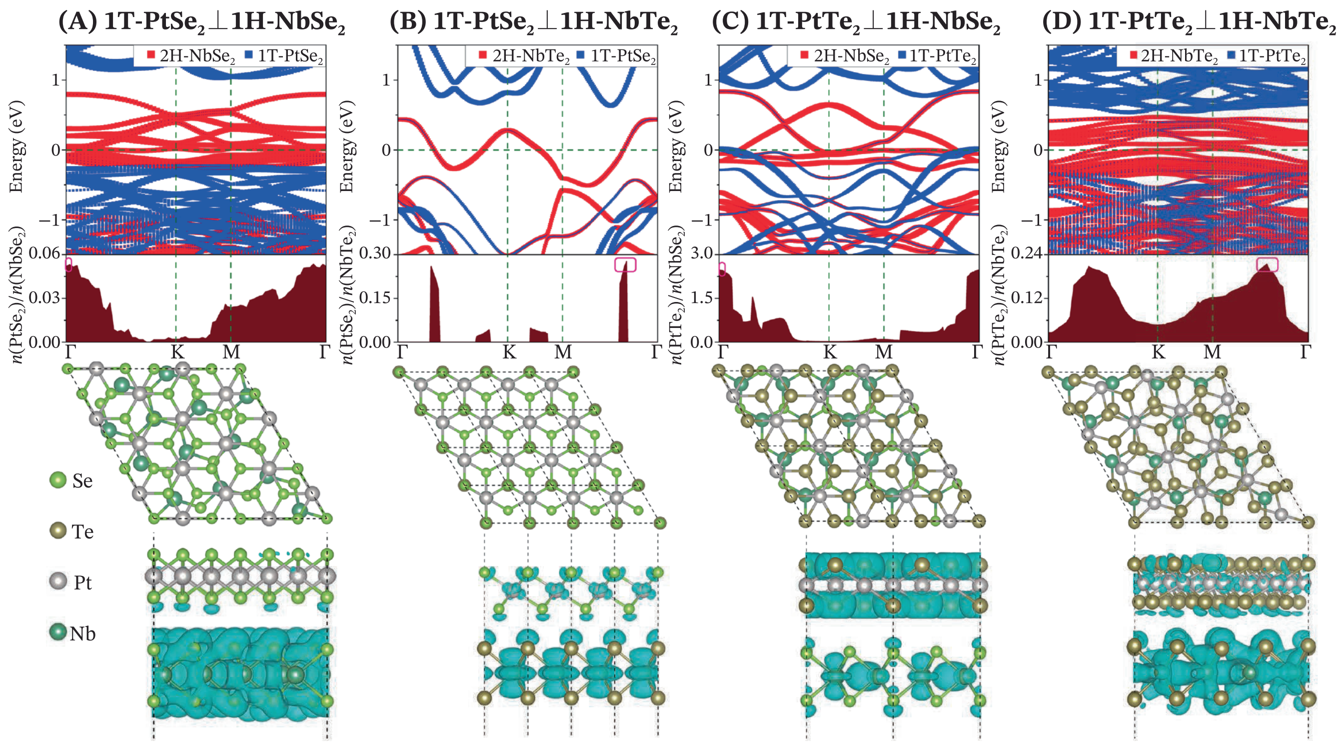

FIGURE 10 Top panels: The projected band structures of (A) 1T-$PtSe_2$⊥1H-$NbSe_2$, (B) 1T-$PtSe_2$⊥1H-$NbTe_2$, (C) 1T-$PtTe_2$⊥1H-$NbSe_2$ and (D) 1T-$PtTe_2$⊥1H-$NbTe_2$ heterostructures using the optB88-vdW functional. Middle panels: The respective total projection ratio of PtX_2 to NbX_2 for the states within 0.1 eV of the Fermi level along the high-symmetry *k*-path. Bottom panels: The top and side views of the respective heterostructure in the most stable stacking configuration. The partial charge associated with the Bloch state marked by a pink round rectangle in the middle panel is superimposed on the side view. The iso-value is set to (A) 0.001 e/Å^3, (B) 0.004 e/Å^3, (C) 0.004 e/Å^3, and (D) 0.0005 e/Å^3, respectively.

1H-NbX_2 near the Fermi level along the high-symmetry *k*-path, as shown in the middle panel of Figure 10. The projection ratio for 1T-$PtTe_2$⊥1H-NbX_2 is generally higher in magnitude than for 1T-$PtSe_2$⊥1H-NbX_2. Although the projection ratio for 1T-$PtSe_2$⊥1H-$NbTe_2$ is comparable to that for 1T-$PtTe_2$⊥1H-$NbTe_2$, the former has fewer electronic states near the Fermi level across the Brillouin zone (see the middle panel of Figure 10B,D). This relative abundance of the contact-induced 1T-PtX_2 states around the Fermi level is further corroborated by the calculated projected density of states in Figure S8. Furthermore, Figure S9 shows the estimated interlayer binding energies, which suggest that 1T-$PtTe_2$ in general binds more strongly with 1H-NbX_2 than 1T-$PtSe_2$. These analyses may suggest that 1T-$PtTe_2$ has better conductivity than 1T-$PtSe_2$ when interfaced with 1H-NbX_2, in line with our experiments. In the bottom panel of Figure 10, we further visualized the partial charge of the Bloch states near the Fermi level at the *k*-point where the projection ratio of 1T-PtX_2 to 1H-NbX_2 is the highest (marked by the pink round rectangle in the middle panel of Figure 10). In the case of the 1T-$PtTe_2$⊥1H-$NbSe_2$ heterostructure, the strong interfacial charge transfer leads to significant partial charge within the 1T-$PtTe_2$ layer. On the other hand, the minor partial charge is observed within the 1T-$PtSe_2$ layer in 1T-$PtSe_2$⊥1H-NbX_2 and the 1T-$PtTe_2$ layer in 1T-$PtTe_2$⊥1H-$NbTe_2$, further manifesting the role of interfacial orbital hybridization in the relatively weak semiconductor-to-metal transition.

3 | CONCLUSION

In conclusion, we have systematically studied the PtX_2/NbX_2 lateral and vertical heterostructures by Raman spectra, XPS, STEM, STM/STS, and DFT calculations. Both pristine semiconducting $PtSe_2$ and $PtTe_2$ are metallized when vertically interfacing with $NbSe_2$ and $NbTe_2$. The metallization of $PtSe_2$ in 1L-$PtSe_2$⊥1L-NbX_2 and $PtTe_2$ in 1L-$PtTe_2$⊥1L-$NbTe_2$ results from the interfacial orbital hybridization, while for $PtTe_2$ in 1L-$PtTe_2$⊥1L-$NbSe_2$ it is due to the *p*-doping effect caused by interfacial charge transfer. This work presents an effective strategy for metallizing NTMDs and provides deep insight into the metallization at an atomic level. Our discoveries could have significant practical applications such as reducing contact resistance at metal electrode/2D semiconductor interfaces and developing devices like 2D Schottky diodes-based rectifiers, rectennas, photodetectors, and so forth, which will be the focus of our future research efforts.

4 | EXPERIMENTAL SECTION/ METHODS

4.1 | Sample preparation

NbX_2 and PtX_2 were grown on HOPG substrates by MBE in an ultrahigh vacuum (UHV) chamber with a base pressure of $\sim 2 \times 10^{-9}$ mbar. Before growth, the freshly cleaved substrate was annealed at 500°C for 2 h. Se and Te (Sigma, 99.99%) were evaporated from Knudsen cells at 150 and 340°C, respectively, while Nb and Pt (ESPI Metals, 99.99%) were evaporated from electron-beam evaporators with their evaporation rates controlled by the flux currents. During growth, the substrate was kept at 280°C, a temperature higher than the sublimation temperatures of Se and Te, and the whole growth process was maintained under Se- or Te-rich conditions to ensure sufficient Se or Te reacting with Nb or Pt. After growth, the sample was cooled to room temperature and capped with Se or Te for ex situ transfer to another UHV system for subsequent STM/STS characterizations. Prior to these measurements, the Se- or Te-capping layer was desorbed at 250°C for 2 h in the preparation chamber of the respective system.

4.2 | STM/STS characterizations

STM/STS measurements were carried out in a multi-chamber UHV system housing an Omicron LT-STM system interfaced to a Nanonis controller at 77 K. The base pressure was better than 10^{-10} mbar. A chemically etched tungsten tip was used, and the bias was applied to the samples. STM images were recorded in constant-current mode.

4.3 | STEM characterizations

The MBE-grown samples were directly lifted from the substrate using a propylene carbonate (PC) film and subsequently transferred onto a TEM grid after being dissolved in dichloromethane. Atomic-resolution STEM-HAADF imaging was conducted at 80 kV using the aberration-corrected JEOL ARM200F equipped with a cold field-emission gun and ASCOR corrector, with a probe convergence semiangle of approximately 30 mrad.

4.4 | Raman characterization

Raman spectra were captured using commercial WITec Alpha 300 R Raman and NT-MDT NTEGR systems. A continuous wave (CW) laser wavelength of 633 nm was used as the excitation source with a spot diameter of $\sim$1 μm using a 100× objective lens (Olympus). For the Raman measurement, a laser power of 0.65 mW with an integration time of 1 s and accumulation times of 2 was used.

4.5 | DFT calculations

All DFT calculations were performed using the Vienna ab initio simulation package (VASP).[58,59] The projector augmented-wave (PAW) method and the optB88-vdW functional were adopted.[60–63] A planewave basis with a kinetic energy cutoff of 450 eV expanded the electronic wavefunction. A Γ-centered *k*-mesh sampled the first Brillouin zone of 1T-PtX_2, 1H-NbX_2, and their heterostructures in such a way that the product of the number of subdivisions with the respective lattice constant is close to 60, while it was set to 1 in the out-of-plane direction. To alleviate the spurious interaction between periodic images in the out-of-plane direction, a vacuum layer of $\sim$20 Å was inserted along that direction. The energy and force convergence criteria were set to 1.0×10^{-5} eV and 0.01 eV/Å, respectively. Anderson's rule, where the vacuum level is the common energy reference, was used to align the band edges of 1T-PtX_2 with the Fermi level of metallic 1H-NbX_2 (Figure S3). Meanwhile, explicit 1T-PtX_2⊥1H-NbX_2 heterostructures were also simulated with the respective supercell models summarized in Table S2. The average in-plane lattice constant was adopted to minimize the strain experienced by both 1T-PtX_2 and 1H-NbX_2 due to the lattice mismatch. Potential stacking configurations of the 1T-PtX_2⊥1H-NbX_2 heterostructure were considered (Figures S4–S6). Here, the AA, AB and AC stacking of 1T-PtX_2⊥1H-NbX_2 indicates that the bottom-layer X, the middle-layer Pt, and the top-layer X of the top 1T-PtX_2 is aligned with the top-layer X of the bottom 1H-NbX_2, respectively. The most stable configuration for each 1T-PtX_2⊥1H-NbX_2 heterostructure was adopted to further perform the electronic structure calculations (Figure 10). The interlayer binding energy of the vertical heterostructure 1T-PtX_2⊥1H-NbX_2 is defined as $E_b(1\mathrm{T}-\mathrm{PtX}_2 \perp 1\mathrm{H}-\mathrm{NbY}_2) = \frac{E(1\mathrm{T}-\mathrm{PtX}_2 \perp 1\mathrm{H}-\mathrm{NbY}_2)-E(1\mathrm{T}-\mathrm{PtX}_2)-E(1\mathrm{H}-\mathrm{NbY}_2)}{A}$, where $E(1\mathrm{T}-\mathrm{PtX}_2 \perp 1\mathrm{H}-\mathrm{NbY}_2)$, $E(1\mathrm{T}-\mathrm{PtX}_2)$, and $E(1\mathrm{H}-\mathrm{NbY}_2)$ are the total energy of the vertical heterostructure 1T-PtX_2⊥1H-NbX_2, and monolayer 1T-PtX_2 and 1H-NbX_2, respectively. A stands for the interfacial area.

ACKNOWLEDGMENTS

L.Z. acknowledges his wife Hongxia for her understanding, support, and love. Without her, this work could not have been completed. L.Z. thanks Mr. Zhang Huanle for his support in the manufacturing of experimental tools. L.Z. and A.T.S.W. acknowledge the Ministry of Education Singapore for funding under grant MOE-T2EP50122-0020. We acknowledge the National Supercomputing Centre Singapore for the computational resources.

CONFLICT OF INTEREST STATEMENT

The authors declare no conflict of interest.

ORCID

Lei Zhang https://orcid.org/0000-0001-5112-6189
Zheng Liu https://orcid.org/0000-0002-8825-7198

REFERENCES

1. Wang Y, Sarkar S, Yan H, Chhowalla M. Critical challenges in the development of electronics based on two-dimensional transition metal dichalcogenides. *Nat Electron*. 2024;7(8):638-645.
2. Zhang X, Liu B, Gao L, et al. Near-ideal van der Waals rectifiers based on all-two-dimensional Schottky junctions. *Nat Commun*. 2021;12(1):1522.
3. Liu Q, Li JJ, Wu D, et al. Gate-controlled reversible rectifying behavior investigated in a two-dimensional MoS_2 diode. *Phys Rev B*. 2021;104(4):045412.
4. Zhang X, Grajal J, Vazquez-Roy JL, et al. Two-dimensional MoS_2-enabled flexible rectenna for Wi-Fi-band wireless energy harvesting. *Nature*. 2019;566(7744):368-372.
5. Gao Z, Zhou Z, Tománek D. Degenerately doped transition metal dichalcogenides as ohmic homojunction contacts to transition metal dichalcogenide semiconductors. *ACS Nano*. 2019; 13(5):5103-5111.
6. Hemanjaneyulu K, Kumar J, Shrivastava M. MoS_2 doping using potassium iodide for reliable contacts and efficient FET operation. *IEEE Trans Electron Devices*. 2019;66(7):3224-3228.
7. Fang H, Tosun M, Seol G, et al. Degenerate *n*-doping of few-layer transition metal dichalcogenides by potassium. *Nano Lett*. 2013;13(5):1991-1995.
8. Jiang J, Xu L, Du L, et al. Yttrium-doping-induced metallization of molybdenum disulfide for ohmic contacts in two-dimensional transistors. *Nat Electron*. 2024;7(7):545-556.
9. Kappera R, Voiry D, Yalcin SE, et al. Phase-engineered low-resistance contacts for ultrathin MoS_2 transistors. *Nat Mater*. 2014;13(12):1128-1134.
10. Zhu J, Wang Z, Yu H, et al. Argon plasma induced phase transition in monolayer MoS_2. *J Am Chem Soc*. 2017;139(30):10216-10219.
11. Gan X, Lee LYS, Wong KY, et al. 2H/1T phase transition of multilayer MoS_2 by electrochemical incorporation of S vacancies. *ACS Appl Energy Mater*. 2018;1(9):4754-4765.
12. Kappera R, Voiry D, Yalcin SE, et al. Metallic 1T phase source/drain electrodes for field effect transistors from chemical vapor deposited MoS_2. *APL Mater*. 2014;2(9):092516.
13. Xu X, Liu S, Han B, et al. Scaling-up atomically thin coplanar semiconductor-metal circuitry via phase engineered chemical assembly. *Nano Lett*. 2019;19(10):6845-6852.
14. Ma R, Zhang H, Yoo Y, et al. $MoTe_2$ lateral homojunction field-effect transistors fabricated using flux-controlled phase engineering. *ACS Nano*. 2019;13(7):8035-8046.
15. Zhang X, Jin Z, Wang L, et al. Low contact barrier in 2H/1T′ $MoTe_2$ in-plane heterostructure synthesized by chemical vapor deposition. *ACS Appl Mater Interfaces*. 2019;11(13):12777-12785.
16. Lee RS, Kim D, Pawar SA, Kim TW, Shin JC, Kang SW. Van der Waals epitaxy of high-mobility polymorphic structure of Mo_6Te_6 nanoplates/$MoTe_2$ atomic layers with low Schottky barrier height. *ACS Nano*. 2019;13(1):642-648.
17. Shen PC, Su C, Lin Y, et al. Ultralow contact resistance between semimetal and monolayer semiconductors. *Nature*. 2021;593(7858):211-217.
18. Chou AS, Wu T, Cheng CC, et al. Antimony semimetal contact with enhanced thermal stability for high performance 2D electronics. *IEEE Int Electron Devices Meet*. 2021;IEDM21:150-153.
19. Li W, Gong X, Yu Z, et al. Approaching the quantum limit in two-dimensional semiconductor contacts. *Nature*. 2023; 613(7943):274-279.
20. Pi L, Li L, Liu K, Zhang Q, Li H, Zhai T. Recent progress on 2D noble-transition-metal dichalcogenides. *Adv Funct Mater*. 2019; 29(51):1904932.
21. Mu H, Yuan J, Lin S. Two-dimensional group-10 noble-transition-metal dichalcogenides photodetector. *Light-Emitting Diodes and Photodetectors-Advances and Future Directions*. IntechOpen; 2021.
22. Wang Y, Zhou L, Zhong M, Liu Y, Xiao S, He J. Two-dimensional noble transition-metal dichalcogenides for nanophotonics and optoelectronics: status and prospects. *Nano Res*. 2022;15(4):3675-3694.
23. Zhao Y, Qiao J, Yu P, et al. Extraordinarily strong interlayer interaction in 2D layered PtS_2. *Adv Mater*. 2016;28(12):2399-2407.
24. Oyedele AD, Yang S, Liang L, et al. $PdSe_2$: pentagonal two-dimensional layers with high air stability for electronics. *J Am Chem Soc*. 2017;139(40):14090-14097.
25. Zhang G, Amani M, Chaturvedi A, et al. Optical and electrical properties of two-dimensional palladium diselenide. *Appl Phys Lett*. 2019;114(25):253102.
26. Xie C, Jiang S, Gao Y, et al. Giant thickness-tunable bandgap and robust air stability of 2D palladium diselenide. *Small*. 2020;16(19):2000754.
27. Zeng LH, Wu D, Lin SH, et al. Controlled synthesis of 2D palladium diselenide for sensitive photodetector applications. *Adv Funct Mater*. 2019;29(1):1806878.
28. Zhang L, Yang T, Sahdan MF, et al. Precise layer-dependent electronic structure of MBE-grown $PtSe_2$. *Adv Electron Mater*. 2021;7(11):2100559.
29. Li J, Kolekar S, Ghorbani-Asl M, et al. Layer-dependent band gaps of platinum dichalcogenides. *ACS Nano*. 2021;15(8): 13249-13259.
30. Li J, Kolekar S, Xin Y, et al. Thermal phase control of two-dimensional Pt-chalcogenide (Se and Te) ultrathin epitaxial films and nanocrystals. *Chem Mater*. 2021;33(20):8018-8027.

31. Zhang L, Yang T, Arramel N, Feng YP, Wee ATS, Wang Z. MBE-grown ultrathin $PtTe_2$ films and their layer-dependent electronic structures. *Nanoscale*. 2022;14(20):7650-7658.
32. Lin MK, Villaos RAB, Hlevyack JA, et al. Dimensionality-mediated semimetal–semiconductor transition in ultrathin $PtTe_2$ films. *Phys Rev Lett*. 2020;124(3):036402.
33. Khan A, Din HU, Idrees M, et al. First-principles study of metal-semiconductor contact between MX_2 ($M = Nb$, Pt; $X = S$, Se) monolayers. *Phys Lett A*. 2019;383(30):125867.
34. Ryu GH, Chen J, Wen Y, Warner JH. In-situ atomic-scale dynamics of thermally driven phase transition of 2D few-layered 1T $PtSe_2$ into ultrathin 2D nonlayered PtSe crystals. *Chem Mater*. 2019;31(23):9895-9903.
35. Zhang K, Wang M, Zhou X, et al. Growth of large scale PtTe, $PtTe_2$ and $PtSe_2$ films on a wide range of substrates. *Nano Res*. 2021;14(6):1663-1667.
36. Lasek K, Li J, Ghorbani-Asl M, et al. Formation of in-plane semiconductor-metal contacts in 2D platinum telluride by converting $PtTe_2$ to Pt_2Te_2. *Nano Lett*. 2022;22(23):9571-9577.
37. Lasek K, Ghorbani-Asl M, Pathirage V, Krasheninnikov AV, Batzill M. Controlling stoichiometry in ultrathin van der Waals films: $PtTe_2$, Pt_2Te_3, Pt_3Te_4, and Pt_2Te_2. *ACS Nano*. 2022;16(6):9908-9919.
38. Pathirage V, Rajapakse RN, Lasek K, Píš I, Bondino F, Batzill M. Thermal- and air-stability of the compositional variants of van der Waals Pt-telluride thin films probed by high resolution photoemission spectroscopy. *Appl Surf Sci*. 2024;644:158785.
39. Ganguli SC, Vaňo V, Kezilebieke S, Lado JL, Liljeroth P. Confinement-engineered superconductor to correlated-insulator transition in a van der Waals monolayer. *Nano Lett*. 2022;22(5):1845-1850.
40. Liu M, Leveillee J, Lu S, et al. Monolayer 1T-$NbSe_2$ as a 2D-correlated magnetic insulator. *Sci Adv*. 2021;7(47):eabi6339.
41. Liu L, Yang H, Huang Y, et al. Direct identification of Mott Hubbard band pattern beyond charge density wave superlattice in monolayer 1T-$NbSe_2$. *Nat Commun*. 2021;12(1):1978.
42. Nakata Y, Sugawara K, Shimizu R, et al. Monolayer 1T-$NbSe_2$ as a Mott insulator. *NPG Asia Mater*. 2016;8(11):e321.
43. Taguchi T, Sugawara K, Oka H, et al. Charge order with unusual star-of-David lattice in monolayer $NbTe_2$. *Phys Rev B*. 2023;107(4):L041105.
44. Bai Y, Jian T, Pan Z, et al. Realization of multiple charge-density waves in $NbTe_2$ at the monolayer limit. *Nano Lett*. 2023;23(6):2107-2113.
45. Du M, Cui X, Yoon HH, et al. Switchable photoresponse mechanisms implemented in single van der Waals semiconductor/metal heterostructure. *ACS Nano*. 2022;16(1):568-576.
46. Jin H, Wei T, Huang B. Incognizant 1T/1H charge-density-wave phases in monolayer $NbTe_2$. *Nano Lett*. 2024;24(35):10892-10898.
47. Naik S, Pradhan GK, Bhat SG, et al. The effect of Sn intercalation on the superconducting properties of 2H–$NbSe_2$. *Physica C*. 2019;561:18-23.
48. Xi X, Zhao L, Wang Z, et al. Strongly enhanced charge-density-wave order in monolayer $NbSe_2$. *Nat Nanotechnol*. 2015;10(9):765-769.
49. Chen C, Das P, Aytan E, et al. Strain-controlled superconductivity in few-layer $NbSe_2$. *ACS Appl Mater Interfaces*. 2020;12(34):38744-38750.
50. Barajas-Aguilar AH, Irwin JC, Garay-Tapia AM, et al. Crystalline structure, electronic and lattice-dynamics properties of $NbTe_2$. *Sci Rep*. 2018;8(1):16984.
51. Li S, Dong Q, Feng J, et al. Evolution of structural and electronic properties in $NbTe_2$ under high pressure. *Inorg Chem*. 2021;60(11):7857-7864.
52. Jia L, Huo CF, Yan XQ, et al. Ultrafast carrier dynamics in 2D $NbTe_2$ films: implications for photonic and optoelectronic devices. *ACS Appl Nano Mater*. 2022;5(12):17348-17355.
53. Yan M, Wang E, Zhou X, et al. High quality atomically thin $PtSe_2$ films grown by molecular beam epitaxy. *2D Mater*. 2017;4(4):045015.
54. O'Brien M, McEvoy N, Motta C, et al. Raman characterization of platinum diselenide thin films. *2D Mater*. 2016;3(2):021004.
55. Ma H, Chen P, Li B, et al. Thickness-tunable synthesis of ultrathin type-II Dirac semimetal $PtTe_2$ single crystals and their thickness-dependent electronic properties. *Nano Lett*. 2018;18(6):3523-3529.
56. Yang Y, Zhang K, Zhang L, et al. Controllable growth of type-II Dirac semimetal $PtTe_2$ atomic layer on Au substrate for sensitive room temperature terahertz photodetection. *Inf Dent*. 2021;3(6):705-715.
57. Nakata Y, Sugawara K, Ichinokura S, et al. Anisotropic band splitting in monolayer $NbSe_2$: implications for superconductivity and charge density wave. *NPJ 2D Mater Appl*. 2018;2(1):12.
58. Kresse G, Hafner J. Ab initio molecular dynamics for liquid metals. *Phys Rev B*. 1993;47(1):558-561.
59. Kresse G, Hafner J. Ab initio molecular dynamics for open-shell transition metals. *Phys Rev B*. 1993;48(17):13115-13118.
60. Blöchl PE. Projector augmented-wave method. *Phys Rev B*. 1994;50(24):17953-17979.
61. Klimeš J, Bowler DR, Michaelides A. Chemical accuracy for the van der Waals density functional. *J Phys Condens Matter*. 2010;22(2):022201.
62. Dion M, Rydberg H, Schröder E, Langreth DC, Lundqvist BI. Van der Waals density functional for general geometries. *Phys Rev Lett*. 2004;92(24):246401.
63. Román-Pérez G, Soler JM. Efficient implementation of a van der Waals density functional: application to double-wall carbon nanotubes. *Phys Rev Lett*. 2009;103(9):096102.

SUPPORTING INFORMATION

Additional supporting information can be found online in the Supporting Information section at the end of this article.

How to cite this article: Zhang L, Zhou X, Yang T, et al. Semiconductor-to-metal transition in platinum dichalcogenides induced by niobium dichalcogenides. *InfoMat*. 2025;7(6):e70010. doi:10.1002/inf2.70010